

Learning continuous SOC-dependent thermal decomposition kinetics for Li-ion cathodes using KA-CRNNs

Benjamin C. Koenig and Sili Deng*

*Department of Mechanical Engineering, Massachusetts Institute of Technology,
77 Massachusetts Ave, Cambridge, MA 02139, United States.*

(Dated: December 18, 2025)

Thermal runaway in lithium-ion batteries is strongly influenced by the state of charge (SOC). Existing predictive models typically infer scalar kinetic parameters at a full SOC or a few discrete SOC levels, preventing them from capturing the continuous SOC dependence that governs exothermic behavior during abuse conditions. To address this, we apply the Kolmogorov-Arnold Chemical Reaction Neural Network (KA-CRNN) framework to learn continuous and realistic SOC-dependent exothermic cathode-electrolyte interactions. We apply a physics-encoded KA-CRNN to learn SOC-dependent kinetic parameters for cathode-electrolyte decomposition directly from differential scanning calorimetry (DSC) data. A mechanistically informed reaction pathway is embedded into the network architecture, enabling the activation energies, pre-exponential factors, enthalpies, and related parameters to be represented as continuous and fully interpretable functions of the SOC. The framework is demonstrated for NCA, NM, and NMA cathodes, yielding models that reproduce DSC heat-release features across all SOCs and provide interpretable insight into SOC-dependent oxygen-release and phase-transformation mechanisms. This approach establishes a foundation for extending kinetic parameter dependencies to additional environmental and electrochemical variables, supporting more accurate and interpretable thermal-runaway prediction and monitoring.

I. INTRODUCTION

Lithium-ion batteries are a key technology for meeting evolving global energy demands. As their prevalence continues to rise, it has become increasingly important to properly quantify and control their safety against catastrophic thermal runaway. Thermal, electrical, and mechanical abuse all provide pathways that lead to accelerating exothermic behavior, heat-releasing internal short circuits, and even extreme combustion events [1]. Reliable and robust models for these phenomena are a key piece in thermal runaway prevention and mitigation.

Differential scanning calorimetry (DSC) is widely used to develop kinetic models that describe component-specific reaction pathways, from standard operating conditions to extreme thermal events. These can include cathode decomposition [2–4], solid electrolyte interphase degradation and regeneration [5, 6], and anode-electrolyte interactions [6, 7], among other minor components and major cross-component interactions. The Kissinger method is a traditional technique for the extraction of kinetic model parameters from these component-scale DSC datasets [5, 8, 9], although it has been shown generally [10, 11] as well as in lithium-ion battery kinetic models specifically [3] that the simplifying assumptions required for its use severely limit its accuracy and capability when attempting to model realistic chemical pathways. Chemical Reaction Neural Networks (CRNN), originally proposed for general autonomous kinetic model discovery [12], have been leveraged extensively as a high-accuracy alternative with the capability for complex and realistic chemical physics inference via their combination of machine learning optimization with the Arrhenius and mass action laws [3, 4, 7, 13, 14]. However, existing CRNN-based models treat kinetic parameters as fixed scalars and therefore cannot represent dependencies on external conditions that are not already represented in the Arrhenius and mass action laws.

State of charge (SOC) is a particularly important external factor because it strongly influences both global and component-scale thermal runaway severity. Increased SOC elevates internal short circuit energy release [15], and similarly cathode materials exhibit greater exothermicity at higher SOCs (higher delithiation levels), both in electrolyte-containing [16, 17] and electrolyte-free settings [16, 18]. Despite this well-established dependence, most kinetic modeling efforts focus exclusively on 100% SOC to generate conservative worst-case safety predictions [2, 6, 7]. Although practical, this approach cannot capture the continuous variation in exothermic behavior that occurs across realistic operating and storage conditions, limiting the predictive capability of such models at realistic, intermediate SOC conditions.

Recent attempts to introduce SOC sensitivity into kinetic modeling have followed two main directions. One approach applies Kissinger-type parameter fitting independently at a limited number of discrete SOC values [19, 20].

* Corresponding author, silideng@mit.edu

These studies provide valuable insight into overall SOC trends but retain the limitations of the underlying analytical framework and do not produce a continuous representation suitable for real-time prediction. A second, more recent approach employs CRNNs with accelerating rate calorimetry (ARC) data to infer SOC-sensitive global heat release and gas evolution [14]. This method achieves strong predictive performance of global thermal runaway trends and is able to accurately model the SOC behavior of the full cell. However, the low resolution and mixed-component nature of ARC data restricts the identifiability of component-specific pathways and intermediate species, and requires the use of lumped reactants with limited correlation to realistic decomposition phenomena. As a result, the inferred models cannot provide mechanistic interpretability or component-resolved decomposition kinetics.

Parallel DSC studies sweeping SOC at fine resolution have revealed a striking phenomenon: the total heat released by mixed cathode-electrolyte samples increases gradually with SOC until a critical value is reached, beyond which the heat release and DSC peak shapes change abruptly and thermal stability rapidly drops [18]. This critical SOC appears to identify a regime transition with significant implications for battery operation, storage, and safety management optimization. Prior work has associated this behavior with sharply increasing lattice oxygen release from nickel-rich cathodes at similar elevated SOCs [21–25]. This oxygen release accelerates exothermic decomposition and electrolyte oxidation, suggesting a mechanistic link between SOC, oxygen evolution, and thermal runaway propensity. However, no existing kinetic framework provides a continuous and fully interpretable SOC-dependent representation of these processes.

The recently proposed Kolmogorov-Arnold Chemical Reaction Neural Network (KA-CRNN) framework [26] offers a means to address this gap. KA-CRNN integrates the mechanistic structure of CRNNs with the functional expressiveness of Kolmogorov-Arnold Networks [27, 28] and Neural ODE formulations [29–31]. The resulting architecture enables Arrhenius parameters to vary smoothly with SOC while remaining anchored in physically constrained reaction networks. In this work, we construct a KA-CRNN model based on literature-supported cathode decomposition and electrolyte oxidation pathways and apply it to nickel cobalt aluminum, nickel manganese aluminum, and nickel manganese cathodes. By learning kinetic parameters directly from DSC measurements across a range of SOC values, the KA-CRNN produces a continuous, mechanistically grounded model that captures the experimentally observed critical SOC behavior [18] and provides component-specific predictive capability for exothermic reactions relevant to thermal runaway under realistic operating and storage conditions.

II. METHODOLOGY

Section II A of the methodology reviews the literature and selects a reasonable model form to capture key SOC dependence behavior in cathode-electrolyte decomposition models. Then, Sec. II B introduces the KA-CRNN formulation to learn the parameterized behavior of this model. We finally introduce the training methodology and datasets in Sec. II C.

A. Cathode-Electrolyte decomposition modeling overview

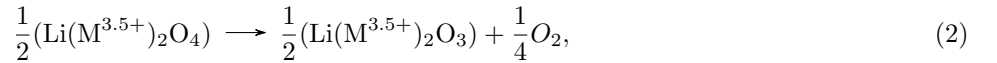
Typical cathode decompositions models developed in the thermal runaway literature, both via analytical techniques [2, 6, 15] and CRNNs [3, 4, 7], report one to three decomposition steps that correspond to global phase change reactions. In NCM cathodes for example, an established pathway involves the pristine layered structure, two sequential spinel structures, and the final rock salt [2, 3, 32]. Such modeling efforts deliver compact models with scalar parameters by limiting inference to a single SOC only. A well-known product of these decomposition reactions is oxygen gas [21, 24, 33], which can oxidize the electrolyte and lead to severe exothermic behavior [34, 35] including fire and explosion [36, 37].

The key recent result motivating the modeling effort of this work was the observation of a critical SOC in cathode-electrolyte DSC samples above which there is a sharp increase in exothermic behavior accompanied by a sudden narrowing of the heat release peak [18]. This observation was made identically across 15 different nickel-rich cathode chemistries, indicating its prevalence in modern battery systems. The seemingly discontinuous nature of this abrupt shift in thermal decomposition behavior, with otherwise well-behaved and smooth trends at lower SOCs, suggests an underlying physical process that similarly responds suddenly to high SOCs rather than gradually at all values. Proper treatment of this underlying process could be the key to enabling highly informative, physics-based kinetic models that respond continuously to the SOC and enable higher-performance monitoring systems. We discuss the chemical and electrochemical origins of this behavior in the two subsections below, starting with the SOC dependence of oxygen evolution from the cathode active material during phase transition and then continuing to electrolyte oxidation and combustion pathways that are highly coupled to the released oxygen.

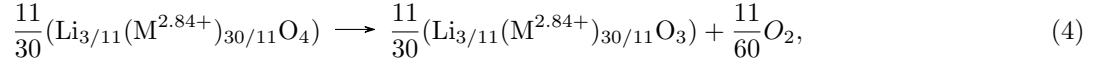
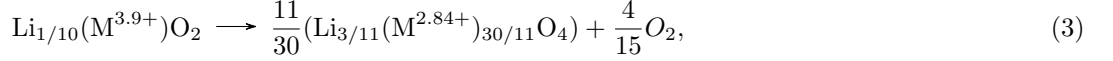
1. Cathode oxygen evolution dependence on lithiation

We begin with discussion of cathode electrochemical decomposition behavior during standard cycling operation, where phase transitions similar to those experienced during thermal abuse are commonly observed. Prior study on the irreversible cycling transformation of surface lattice structures for NCM cathodes [22] concluded that the type of phase change decomposition experienced at the surface of the cathode depends on the voltage condition: at elevated but still relatively low voltages corresponding to a half or more delithiated cathode, the observed cycling phase change is to the spinel structure, with little to no oxygen release. Heavily delithiated voltages near 4.8V, meanwhile, favor complete decomposition to the rock salt phase due to the highly oxidative environment. This high-voltage decomposition notably releases significant amounts of oxygen. Modeling of this surface reconstruction [38] has similarly concluded that the key degradation behavior (and implicitly the oxygen release characteristics) are governed by an electrochemical voltage cutoff rather than a smooth trend: below 4.4V the model computed zero surface reconstruction or capacity fade, while above 4.4V standard cycling led to phase change and degradation.

On the thermal side of the literature, TGA-MS studies [21] on an array of uncoated, coated, single crystal, and polycrystalline NCM cathodes of varying nickel ratios charged to 4.2, 4.4, and 4.6V arrived at a similar conclusion: little to no oxygen evolution was measured at 4.2V, with significant increases at 4.4V and 4.6V. Another gas evolution study [24] corroborates these results with its own experimental data and further proposes a set of two-step reactions for nickel-rich NCM cathodes at varying lithiation levels. We reproduce the lowest-charge (lithiated pristine cathode) pathway first,



with the top reaction representing the phase change from the layered cathode to the spinel phase, and the bottom reaction representing the spinel phase to rock salt decomposition. Notable here is the lack of oxygen production during the first decomposition step, and the minor oxygen production at the second step. In contrast, the highest-charge pathway (delithiated pristine cathode), reproduced again from [24], is as follows:



where similar overall steps but adjusted stoichiometry and charge balances lead to significant oxygen release in the first step and an 80% increase in total production. We gather from this series of electrochemical and thermal cathode studies that there is significant experimental justification for a sharp increase in oxygen released from the cathode at high SOCs (or proportionally, high voltages). In the next section, we connect this oxygen evolution to exothermic behavior at the electrolyte, and propose a KA-CRNN model form to bring these behaviors together in a cohesive numerical model that can explain the critical SOC phenomenon using these real chemical physics behaviors.

2. Electrolyte oxidation and proposed model form

Further theory is needed to correlate this sudden oxygen release increase with the critical exothermic safety behavior observed in [18], where DSC samples included cathode samples mixed with liquid electrolyte. Electrolyte oxidation has been widely studied in chemical and electrochemical settings [23, 25, 39], where the electrochemical pathway via carbonate dehydrogenation occurs relatively slowly at extreme voltages, and the chemical oxidation pathway that relies on cathode-released oxygen is known to increase in rate suddenly at still elevated but relatively lower voltages [25]. This connection between cathode-evolved oxygen and electrolyte oxidation or combustion, and its significant impact on practical-scale thermal runaway, has been well-studied [34–37, 40, 41], and provides a strong link between the sudden increase in oxygen evolution described in Sec. II A 1 and the seemingly related sudden increase in cathode-electrolyte heat release [18]. We theorize in this work that proper, continuous treatment of the evolved oxygen stoichiometry is the key to developing a truly global, SOC-varying model for this cathode-electrolyte exothermic behavior, and may help to lay the groundwork for extended applications in other battery materials.

We briefly remark that the results reviewed here are not fully consistent on whether the oxygen evolution in cathode materials depends on the SOC or voltage. Some work has even suggested that the true answer is neither, and that

the differential capacity (dq/dV) is the fundamental predictor of such behavior [25]. While perfect correlations do not exist due to transient effects and overpotentials, rough conversions of all metrics via charging curves [18] reveal that all effects discussed here occur in similar ranges across all three variables. For the purposes of this study, we select the SOC as the dependent variable, but note that with controlled experiments the voltage and differential capacity are also suitable choices and that further investigation here may reveal new insights.

General conclusions of the above review are as follows:

1. Thermal decomposition of layered nickel-rich cathodes occurs in at least two steps, through the spinel and rock salt phases. Proper modeling efforts must account for variation in oxygen release across these steps.
2. The bulk of the oxygen release occurs in the second step, in quantities generally agreed upon in the literature to vary significantly with the SOC.
3. The released oxygen reacts strongly with the electrolyte, producing significant exothermic behavior. We find no consensus in the literature suggesting that the electrolyte oxidation kinetics vary significantly with the SOC.
4. Reported voltage and SOC thresholds in the literature indicate that the critical SOC for thermal safety [18] occurs at the same SOC as sudden increases in cathode oxygen evolution. This suggests that a model properly accounting for the SOC-based variation in cathode oxygen evolution will inherently be capable of predicting SOC-dependent exothermic effects.

Following from these points, we propose the following simple model form for general nickel-rich exothermic cathode decomposition:



Here C_l is the pristine layered cathode structure, C_s is the spinel structure, and C_r is the rock salt for a generic nickel-rich material. O_2 is also present in the system, as is C_{prod} , the product of the reaction between O_2 and the electrolyte C_e . Enabling even a simple kinetic model like this to respond to the SOC presents a challenge. The rate parameters of the electrochemically-dependent R1 and R2 differ for each studied cathode chemistry, and also must respond continuously to the SOC. R3', meanwhile, represents the chemical electrolyte oxidation pathway that occurs regardless of cathode or SOC, as indicated by the prime notation. Similarly, the heat released from the first two reactions is SOC dependent, while the prime $\Delta H'_3$ is a fixed constant based on the electrolyte chemistry.

Returning to the four constraints listed above, we note that the the two-step cathode decomposition in R1 and R2 satisfies conclusion (1), the SOC dependent coefficient ν in R2 satisfies (2), the presence of R3 satisfies (3), and KA-CRNN training of the oxygen evolution reaction using critical SOC data will implicitly enforce (4). The continuously varying kinetic parameters of R1 and R2, especially the oxygen stoichiometric coefficient ν , are the key modeling innovation that enable this concise yet still strongly physics-encoded reaction model. To accurately learn these continuous kinetic parameters, we leverage KA-CRNNs as discussed in the next subsection and shown in Fig. 1.

B. Physics-encoded KA-CRNN with O_2 release and electrolyte oxidation

The KA-CRNN approach [26] first involves the definition of a complete CRNN via the Arrhenius and mass action laws [12], as is prevalent in the literature for thermal runaway kinetics [3, 4, 7, 13]. Then, the subset of kinetic parameters defined in the CRNN for R1 and R2 are re-parameterized using KAN activations to incorporate their continuous functional dependence on an external factor, here the SOC. The CRNN reaction system is as defined in Eqs. 5 through 7. The reaction rates can be computed as

$$r_i = \exp(n_i \ln[c_i] + \ln A_i + b_i \ln T - E_{a,i}/RT) \quad (8)$$

for the i^{th} reaction, where $i = 1 : 3$. c_1 is the mass fraction of the layered structure corresponding to C_l , while c_2 is the spinel phase (C_s) and c_3 is the oxygen (O_2). C_r and C_{prod} do not impact any reaction rates and are not tracked in the CRNN learning problem, meanwhile the mass fraction of the electrolyte corresponding to C_e is fixed at unity due to the oxygen-limited reaction, thus it has a constant zero effect on Eq. 8. The individual species production and consumption rates are

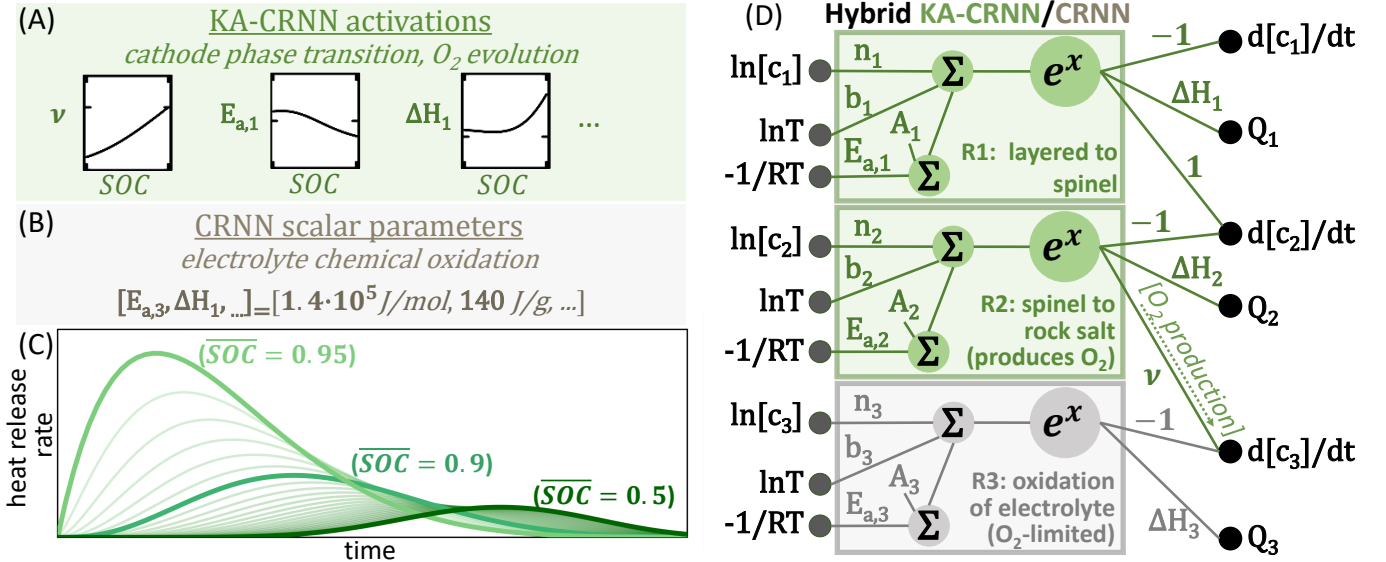


FIG. 1: Overview of KA-CRNN framework for SOC-dependent thermal runaway kinetics. (A) KA-CRNN kinetic parameters, represented as continuous functions of SOC. (B) Standard CRNN kinetic parameters, represented as fixed scalar values without SOC dependence. (C) Example KA-CRNN prediction illustrating the continuous variation of heat-release behavior with SOC. (D) Complete KA-CRNN architecture used in this study. Reactions R1 and R2 are defined by KA-CRNN parameters as in panel (A) and are identified separately for each cathode material. Reaction R3 uses scalar CRNN parameters as in panel (B) and is learned once for all cathodes, but its effective behavior remains SOC dependent through its reliance on O₂ production from R2.

$$\frac{dc_1}{dt} = -r_1, \quad [\text{layered phase}] \quad (9)$$

$$\frac{dc_2}{dt} = -r_2 + r_1, \quad [\text{spinel phase}] \quad (10)$$

$$\frac{dc_3}{dt} = -r_3 + \nu r_2. \quad [\text{evolved } O_2] \quad (11)$$

Finally, the key exothermic heat release term is defined using the individual reaction enthalpies ΔH_r as

$$Q_{tot} = \sum_i Q_i = \sum_i \Delta H_i r_i. \quad (12)$$

The rates reported in Eqs. 9 through 12 can be seen in the one-to-one mapping on the output side of Fig. 1(D). Kinetic parameter responses to the SOC are encoded via univariate KAN activations [27, 29], as originally demonstrated in a proof-of-concept KA-CRNN [26]. The i^{th} SOC-varying kinetic parameter is defined as

$$p_i(\text{SOC}, \boldsymbol{\theta}) = \text{KAN}(\text{SOC}, \boldsymbol{\theta}_i) = \phi_i(\text{SOC}), \quad (13)$$

where thanks to the CRNN handling the coupling to the full-scale kinetic model, the entire KAN that reconstructs p_i is represented by just a single, fully interpretable activation function ϕ_i . This simple encoding facilitates convergence and human-interpretable meaning by isolating the specific effect of the SOC on each individual parameter. The univariate functions are parameterized by the learnable KAN parameters θ and are defined using the Chebyshev KAN formulation [42] as

$$\phi_i(SOC) = \sum_{n=0}^N w_{i,n}^\psi \cdot \psi_n(SOC), \quad (14)$$

$$\psi_n(\text{SOC}) = \cos(n \cdot \arccos(\text{SOC})). \quad (15)$$

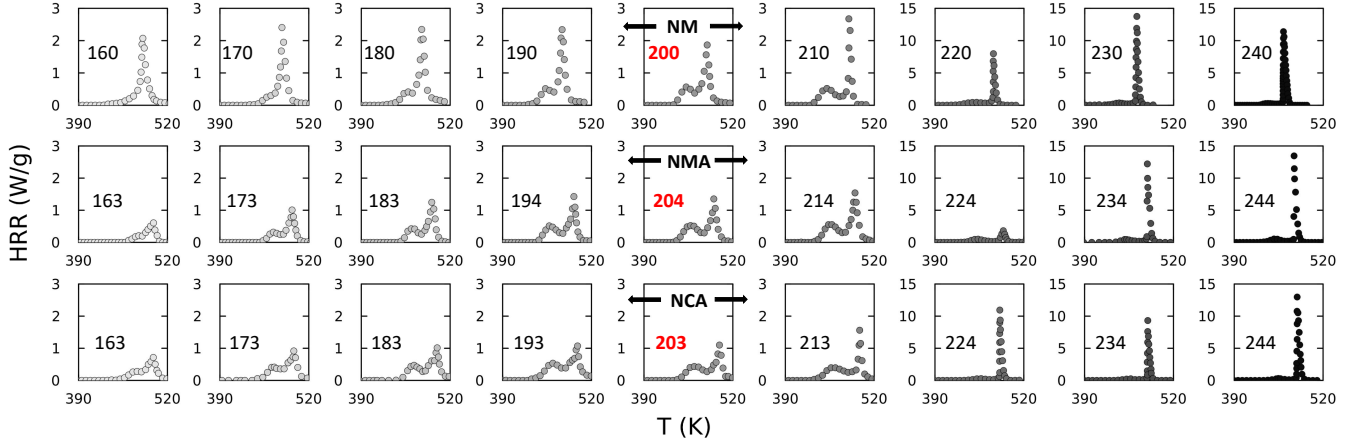


FIG. 2: DSC training data reproduced from [18]. Rows are NM, NMA, and NCA cathode materials from top to bottom. The y-axis scale changes beginning at the seventh column to improve visibility of the substantially increased heat release at elevated SOCs. Individual SOCs are indicated on each subfigure in mAh.

This encoding constructs the complete activation function ϕ_i as the sum of Chebyshev polynomials ψ_n up to degree N . $w_{i,n}^\psi$ contains a learnable scaling parameter for each polynomial degree n of each kinetic parameter i , and makes up the learnable network parameter vector θ . We use the continuous Chebyshev polynomial formulation here rather than the standard gridded basis KAN formulation to accommodate the relatively sparse training data. A unique parameter set θ comprised of the θ_i reconstructing each individual parameter is learned for each studied cathode material (R1 and R2), in addition to a standard set of scalar CRNN parameters for the universal electrolyte oxidation model (R3). This implementation enables a fully continuous, assumption-free representation of the kinetic parameters' responses to the SOC, while retaining the strongly physics-encoded CRNN backbone through which the parameters are integrated to reconstruct the training data. For all parameter activations in this work, we use $N = 10$, which when counting the zeroth degree polynomial term results in eleven KAN parameters used to learn each true kinetic parameter (121 KAN parameters used to fully learn the 11 real kinetic parameters in each cathode's 2-step decomposition pathway). A complete visualization of the model framework is available in Fig. 1.

C. KA-CRNN training: NMA, NM, and NCA cathodes

To demonstrate the versatility and robustness of the KA-CRNN technique, we train on three separate nickel-rich cathode datasets reproduced from [18], all of which experienced the critical SOC phenomenon: nickel cobalt aluminum (NCA), nickel manganese (NM), and nickel manganese aluminum (NMA). Each dataset contains nine DSC experiments at increasing SOCs. For all three cathodes, we withhold the fifth dataset as testing data, to verify that the KA-CRNN is not overfitting the training data. All training data, with testing data labeled in red, is available in Fig. 2.

Returning to the physical system described in Eqs. 5 through 7, we recall that certain reactions and parameters (phase change in the cathode material, R1 and R2) depend on the SOC, while others (electrolyte oxidation chemistry, R3) do not. To properly capture the true underlying chemical physics, the SOC-dependent parameters that define the two cathode phase transformations and the oxygen production rate (Eqs. 5 and 6) are defined uniquely and optimized only to that cathode's DSC data. Meanwhile, the SOC-invariant parameters for the electrolyte oxidation are defined once and optimized across all cathode datasets (Eq. 7). Table I lists all learnable parameters, and whether they are cathode-specific KAN activations or universal scalar values.

Optimization of all kinetic parameters to multiple datasets presents a challenge, especially when coupling cathode-specific and SOC-varying reactions to the universal electrolyte oxidation through ν . To ensure a meaningful converged model, the loss function takes an augmented mean squared error (MSE) formulation with physics-informed penalties,

TABLE I: Classification of all learnable parameters.

Inference technique	Parameters
Cathode-specific KAN activation. Function of SOC. [cathode decomposition and O ₂ production]	$n_1, n_2, A_1, A_2, E_{a,1}, E_{a,2}, b_1, b_2, \Delta H_1, \Delta H_2, \nu$
Universal scalars. SOC-invariant, cathode-invariant. [electrolyte oxidation/combustion]	$n_3, A_3, E_{a,3}, b_3, \Delta H_3$

$$\mathcal{L}(\boldsymbol{\theta}) = \frac{1}{k} \sum_k |Q_{tot,k}^{data} - Q_{tot,k}^{KA-CRNN}| + \mathcal{L}_{mono}(\boldsymbol{\theta}) + \mathcal{L}_{min}(\boldsymbol{\theta}) + \mathcal{L}_{max}(\boldsymbol{\theta}), \quad (16)$$

$$\begin{aligned} \mathcal{L}_{mono}(\boldsymbol{\theta}) = & \sum_{j=2}^9 [\text{Max}(\Delta H_2(\text{SOC}_{j-1}, \boldsymbol{\theta}) - \Delta H_2(\text{SOC}_j, \boldsymbol{\theta}), 0)) \\ & + 10^2 \text{Max}(\nu(\text{SOC}_{j-1}, \boldsymbol{\theta}) - \nu(\text{SOC}_j, \boldsymbol{\theta}), 0)], \end{aligned} \quad (17)$$

$$\mathcal{L}_{min}(\boldsymbol{\theta}) = \text{Max}\left(\frac{1}{n_3} - 1, 0\right) 10 \sum_{j=1}^9 \sum_{k=1}^2 \text{Max}\left(\frac{1}{n_k(\text{SOC}_j, \boldsymbol{\theta})} - 1, 0\right), \quad (18)$$

$$\mathcal{L}_{max}(\boldsymbol{\theta}) = 0.05n_3^4 + b_3^4 + \sum_{j=1}^9 \sum_{k=1}^2 [0.05n_k^2(\text{SOC}_j, \boldsymbol{\theta}) + b_k^3(\text{SOC}_j, \boldsymbol{\theta})]. \quad (19)$$

$\mathcal{L}(\boldsymbol{\theta})$ is the overall loss function that informs model optimization through gradient stepping of the values in $\boldsymbol{\theta}$. In addition to the MSE term computed against the DSC data, $\mathcal{L}_{mono}(\boldsymbol{\theta})$ provides a soft monotonic penalty on the spinel to rock salt reaction enthalpy and the oxygen production stoichiometric coefficient, encouraging but not requiring both to increase across SOCs based on our physical knowledge from Sec. II A of decreased thermal stability at elevated SOCs. These two variables are highly correlated via their overlapping behavior in the second observable heat release peak at all SOCs (Fig. 2), making their inference slightly underconstrained and requiring this $\mathcal{L}_{mono}(\boldsymbol{\theta})$ penalty to avoid overfitting. A similar constraint for the layered to spinel reaction enthalpy is not needed, as those reaction enthalpies are fully constrained by the area under the first observable heat release peak in Fig. 2, with no competing reactions. $\mathcal{L}_{min}(\boldsymbol{\theta})$ provides an increasing penalty on reaction orders less than unity as they approach zero, which helps maintain reasonable rate law formulations and ensure numerical stability. Note that n_3 is treated outside of the sums as it is a scalar value, while the SOC-dependent n_1 and n_2 are sampled at the nine SOCs provided in the data. $\mathcal{L}_{max}(\boldsymbol{\theta})$ similarly provides an increasing penalty for large values of all reaction orders and non-exponential temperature factors, to prevent nonsensical parameterizations. These are especially relevant for the electrolyte oxidation reaction, which given the very narrow peaks at high SOCs is prone to drifting toward extreme parameter values. These loss constraints provide knowledge-based guardrails that ensure a meaningful final model without hampering its interpretability or realistic chemical physics.

KA-CRNN predictions are computed by integrating the governing equations, as parameterized by the KA-CRNN, in the DifferentialEquations package in Julia [43]. Model optimization is carried out by updating model parameters according to the gradients of the loss function as computed via autodifferentiation in the ForwardDiff package [44] in Julia. The ADAM optimizer is used for training [45], with a learning rate of 5×10^{-4} .

III. RESULTS AND DISCUSSION

A. SOC-varying DSC predictions with sparse KA-CRNN model

Reconstructed DSC profiles for the NM cathode plus electrolyte experiments at varying SOCs [18] are shown in the top blue row of Fig. 3(A). Inspection of the three provided training profiles with appropriately scaled y-axes indicates strong performance, with the KA-CRNN's learned responses to the SOC for the two cathode decomposition reactions (R1 and R2) enabling them to change in location, magnitude, and shape as the SOC increases. Also observable are significant changes in the shape, size, and peak temperature of the R3 peak at increasing SOCs, which are notable given its fixed kinetic parameters across all SOCs (and across all cathodes). Instead, these shifts demonstrate the successful

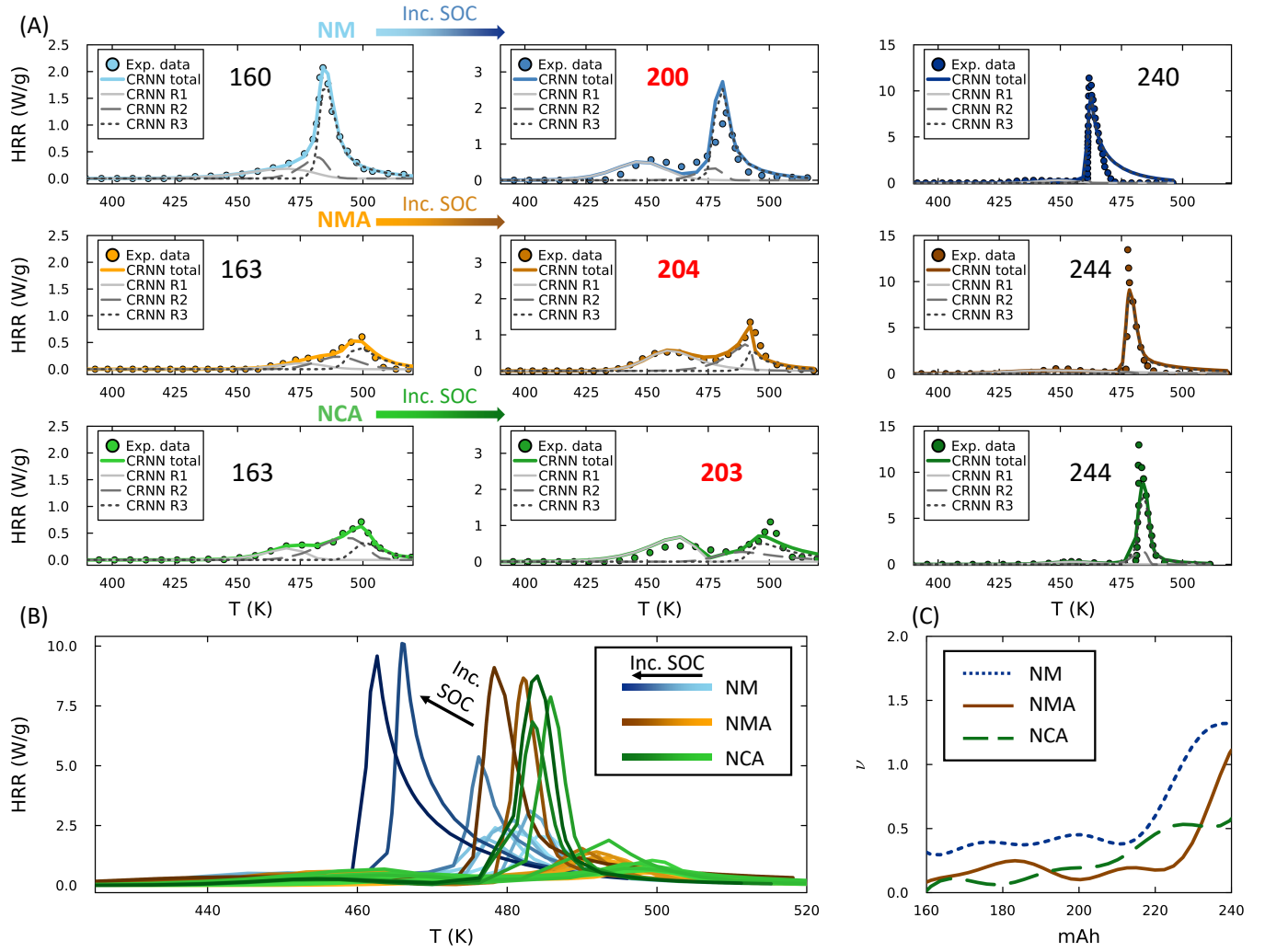


FIG. 3: (A) DSC reconstructions for all three studied cathodes (NM, NMA, and NCA, from top to bottom), at three example SOCs (minimum, testing, and maximum from left to right). SOCs are labeled in mAh (black for training, red for testing). Note y-axes are scaled to each column for visibility. (B) All nine SOCs for all three cathodes plotted together, showing significantly distinct trends in peak heat release, peak heat release temperature, and total heat release as the SOC increases. (C) Oxygen evolution stoichiometric coefficient KA-CRNN activations for each cathode material, highlighting critical SOCs around 210 mAh to 230 mAh across all materials

implementation of two key behaviors in the KA-CRNN: first, the SOC-sensitive oxygen production stoichiometric coefficient (shown in Fig. 3(C)) increases the total oxygen availability at higher SOCs as is well-reported in the literature, enabling R3 to release more heat even with a fixed per-unit-oxygen reaction enthalpy ΔH_3 . Secondly, the limiting oxygen reactant for R3 is produced directly during R2, making R2 initiation a prerequisite for the onset of R3 heat release, and thus making the shape of the R3 heat release peak dependent on the shape of the R2 phase change peak. These two pathways give the KA-CRNN the expressivity needed to control, respectively, the size and onset of R3 through the SOC-dependent R2 kinetics.

Inspection of the blue NM curves in the combined Fig. 3(B) further emphasizes the stark difference in peak heat release, total heat release, and onset temperature as the SOC changes. The learned KA-CRNN activations are successful at capturing this shifting behavior across all SOCs well. The oxygen production stoichiometric coefficient's variation with respect to the SOC is shown in Fig. 3(C), where between 210 mAh and 220 mAh there is a sudden jump in the blue NM profile corresponding to the sudden increase ($> 2\times$) in peak heat release in the reconstructed profiles at those SOCs. This visualization in Fig. 3(C) is available with zero postprocessing thanks to the direct KA-CRNN activation function learning via polynomial basis functions, facilitating highly interpretable results that not only fit the data but also correspond well to the realistic underlying physics. The remaining KA-CRNN parameters (see Table

TABLE II: Learned electrolyte oxidation parameters

$\ln A_3$	$E_{a,3}$	b_3	ΔH_3	n_3
132.45	5.37×10^5	-0.069	1779.39	3.250

I for the complete list) can be visualized similarly, and are discussed in the next section. Finally, we remark that the ability of the KA-CRNN to fit the testing data in the top row of Fig. 3(A) well (200mAh, labeled in red) despite no nearby training points is a significant result for this approach, and emphasizes the continuous yet overfitting-resistant nature of its response to the SOC. The fixed electrolyte oxidation parameters learned across this and the remaining NMA and NCA data are reported in Table II.

Next, the same results are shown for the NMA cathode plus electrolyte DSC data in the orange middle row of Fig. 3. Similar conclusions can be drawn: the responses of R1 and R2 to the SOC are both learned well, and adjust in shape and magnitude as needed to properly fit all training data. R3, despite its SOC-invariant chemistry that is shared with the NM and NCA cases (see parameters in Table II), is still shown to capture all of the experimental peaks well thanks to its dependence on the SOC-sensitive R2 for the reactant oxygen production. The relatively new NMA chemistry [46] is more stable than the cobalt-free NM cathode, which manifests in a lower stoichiometric coefficient at all SOCs as well as a higher critical SOC in the orange curve of Fig. 3(C), leading to less overall electrolyte oxidation and R3 heat release.

The KA-CRNN's ability to reconcile these significant differences between the NMA and NM cathode stabilities even with the constant scalar R3 parameters is notable, and provides interesting kinetic insights. R2 in the NM reconstructions (top blue row), especially at low SOCs, is relatively narrow. All oxygen is produced relatively early by the narrow R2, allowing the Arrhenius rate law for R3 to largely control the electrolyte oxidation behavior. In the NMA cathode, however (middle orange row), the R3 peak occurs at a higher temperature in the data, thanks to the more stable chemistry [46]. The scalar R3 parameters at these higher temperatures predict an exponentially faster reaction due to the Arrhenius rate law, which is not corroborated by the still-broad DSC peaks (especially at low SOCs). To correct for this, the KA-CRNN optimization learns a broader R2 peak for the NMA cathode, evolving smaller quantities of oxygen over a wider temperature window. This wider SOC-dependent R2 peak effectively broadens the high Arrhenius rate R3 peak through a mass action law limitation that restricts oxygen availability. Such discussion highlights a unique capability of the KA-CRNN framework: the KAN activations enable continuous SOC-based modeling, while the strictly physics-enforced CRNN backbone facilitates such direct kinetic interpretation of the real model results.

Extrapolation to the testing data for the NMA cathode is also seen to be strong in Fig. 3(A), as is the ability of the oxygen evolution stoichiometric parameter to capture the critical SOC and accompanying sudden heat release in Fig. 3(C).

We finally demonstrate reconstructed DSC results for the NCA cathode plus electrolyte DSC data in the bottom green row of Fig. 3, offering comparison with a more traditional cathode chemistry. Similarly strong performance is seen in the training reconstructions. The testing reconstruction is not quite as accurate as in the first two cathode materials, but it retains good accuracy and peak location despite the sparse training data. Inspection of all overlaid reconstructions in Fig. 3(B) enables comparison of overall thermal stability trends, where we note that the NCA and NMA are quite similar in their improved thermal stability over the NM. Both release significantly less heat than the NM cathode at lower SOCs, and generally have higher peak heat release temperatures, indicating higher thermal stability. The NCA suffers from a slightly lower critical SOC than the NMA, as can be seen in Fig. 3(C), while the NMA's highest SOC samples suffer from slightly lower peak heat release temperatures (Fig. 3(B)). Full sets of training data reconstructions (i.e., Fig. 3(A) at all SOCs for all cathodes) are available in Appendix B.

B. KA-CRNN parameter visualizations and SOC trends

The learned DSC reconstructions of Fig. 3 resulted in three separate sets of SOC-dependent KA-CRNN kinetic parameters for R1 and R2, as well as a single set of scalar-valued parameters for R3. The latter are shown in Table II, while we plot the KA-CRNN kinetic parameters for the Arrhenius parameters for all three cathodes in Fig. 4 (remaining activations are available in Appendix A). The first phase change reaction's parameters (Figs. 4(A) and (C)) see modest changes across the SOC, which when compared to the fairly consistent R1 behavior seen in the data of Figs. 2 and 3 is to be expected. The second phase change reaction's parameters (Figs. 4(B) and (D)) see significant shifts just before each cathode material's critical SOC, once again corroborating the sudden increase in heat release seen in the underlying DSC data of Figs. 2 and 3, the oxygen stoichiometric parameter's behavior in Fig. 3(C), and the dependence of R3 heat release on R2 activity. These results demonstrate the KA-CRNN framework is able to

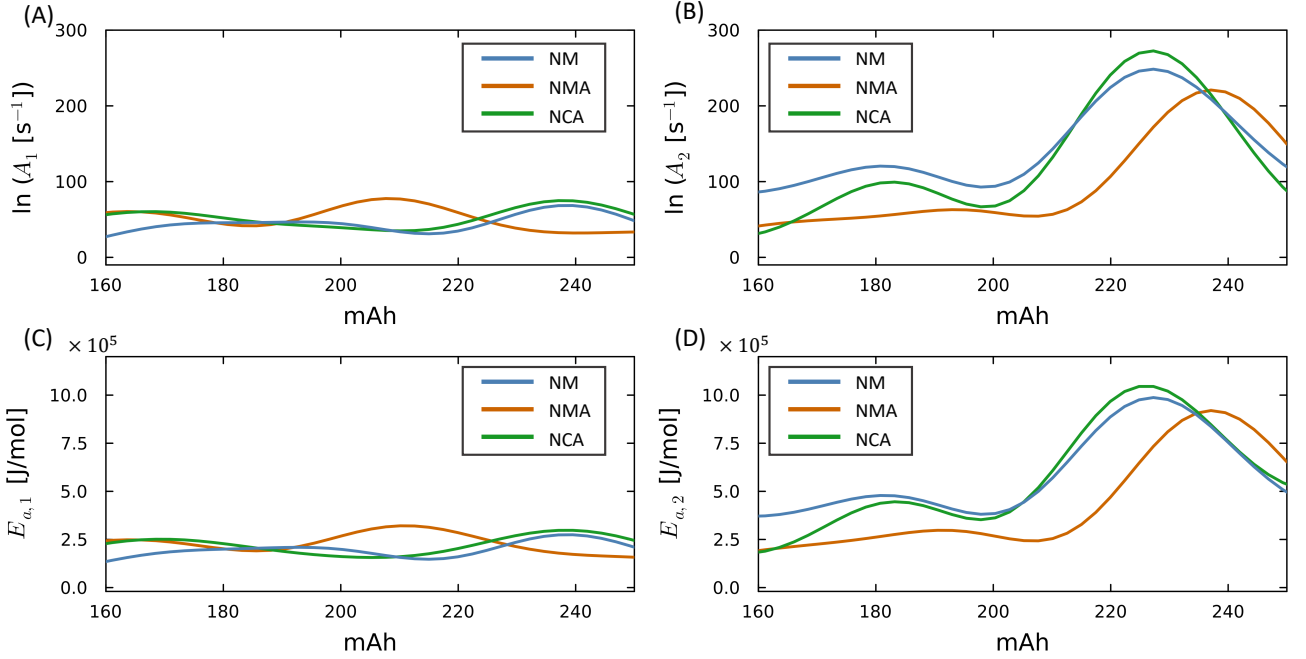


FIG. 4: Learned KA-CRNN activations for the two frequency factors (A-B) and two activation energies (C-D) of all three cathode materials. Note increase in $\ln A_2$ and $E_{a,2}$ occurs at a higher SOC for NMA cathode, corresponding to its higher critical SOC. KA-CRNN activations and discussion for all remaining kinetic parameters are available in Appendix A.

directly learn the underlying chemical behaviors that explain these responses in a visualizable and fully self-consistent manner, in addition to accurately describing the continuous thermal responses of these components to the SOC. Further discussion and visualization of the complete set of activations for all kinetic parameters across all cathodes is available in Appendix A. The numerical values for the continuous parameters are available in the supplementary material.

We finally emphasize that, thanks to the CRNN coupling, the KA-CRNN activation functions learned here are exactly equal to the real kinetic parameters used in the Arrhenius and mass action formulation of Eq. 8. Downstream application of the models developed in this work needs only to refer to the simple activation functions of Figs. A1 through A3 (available in the supplementary materials), which when sampled at any SOC can be integrated forward in time identically to any other thermal-kinetic model.

C. Future outlook

The current study provides a first of its kind model describing the continuous SOC variation of the cathode and electrolyte submodel during thermal runaway with a fully physics-enforced and interpretable set of reactions. Future studies on similar datasets involving all battery components including the anode and separator could facilitate complete, cell-level thermal runaway kinetic models with such physics-based, continuous SOC variation that enable live safety evaluation while retaining strict adherence to fundamentally understood reaction pathways and component interaction effects. KA-CRNNs are also integrable with the previously demonstrated bottom-up Bayesian CRNN approach to cell-level model development based on component DSC data [7, 47], potentially enabling fully descriptive probabilistic models that account for experimental uncertainty in addition to SOC variation.

Thanks to the prior knowledge encoded directly into the reaction model, the currently proposed framework was able to extract a significant amount of realistic model behavior from limited heat release DSC data only, including oxygen evolution stoichiometry. That said, we recognize as well that augmented datasets could aid in further model fidelity. Combined DSC and TGA datasets, for example, could serve to better pin down the oxygen evolution kinetic behavior through mass change loss terms, while the incorporation of mass spectrometry data could also lead to models that continuously report evolved gas species and ratios across SOCs. Nonetheless, the current results already demonstrate the capability of KA-CRNNs to learn SOC-varying thermal runaway kinetic models from fairly sparse data thanks to their incorporation of the cathode-electrolyte reaction physics across a continuous range of SOCs, retaining full

interpretability of all reactions and tracked species while adhering fully to previously reported chemical pathways.

IV. CONCLUSIONS

This work employed Kolmogorov–Arnold Chemical Reaction Neural Networks to construct state-of-charge dependent kinetic models for cathode decomposition and electrolyte oxidation in lithium-ion batteries, delivering unified predictive models for NM, NMA, and NCA chemistries that remain strongly grounded in realistic chemical physics. A detailed review of the impacts of the SOC on cathode oxygen evolution and electrolyte oxidation provided realistic reaction pathways based on prior experimental results, while a carefully tailored hybrid KA-CRNN structure encoded these pathways into a learnable, interpretable network. KA-CRNN models trained on recently reported experimental data were able to accurately capture all relevant chemical pathways including critical SOCs, oxygen production and electrolyte oxidation, heat release rates, and peak temperature values, with strong generalization capabilities highlighted by validation on withheld testing data at an unseen SOC. The delivered models are able to predict the continuous dependence of these exothermic cathode and electrolyte interactions on a cell’s SOC, potentially facilitating finer and higher-resolution safety monitoring in practical applications, especially under SOC-limited safety regimes where previous 100% SOC models are not applicable.

A key novelty of this approach is the continuous response of the KA-CRNN kinetic parameters to the SOC, a significant departure from standard approaches that use fixed parameters at single or discrete SOCs only. Additionally, the modularity of KA-CRNNs with generic CRNNs and standard rate forms enables the simultaneous inference of a shared, SOC-invariant electrolyte oxidation reaction, providing a more generalizable model with sparser and meaningful parameters that facilitates simpler and more robust training through shared information across different chemistries. KA-CRNNs are a general approach for the modeling and elucidation of unknown external factors through physically-grounded kinetic models, and are not limited to modeling the effects of SOC. In the battery thermal runaway field especially, where there are many global and single-step reactions with murky dependencies on external variables that could include pressure and electrochemical operating conditions, KA-CRNNs show promise in elucidating such relationships and providing accurate, continuous, and interpretable predictive models.

V. DECLARATION OF COMPETING INTEREST

The authors declare that they have no known competing financial interests or personal relationships that could have appeared to influence the work reported in this paper.

VI. ACKNOWLEDGEMENTS

SD acknowledges the support from the National Science Foundation under Grant No. CBET-2143625. BCK is partially supported by the National Science Foundation Graduate Research Fellowship under Grant No. 1745302. This research was supported by the Department of Energy (DOE) under Grant No. DE-EE0011364. The authors would like to thank Professor Martin Bazant for his expertise on cathode phase transformation theory.

CREDIT AUTHORSHIP CONTRIBUTION STATEMENT

Benjamin C. Koenig: Conceptualization, Methodology, Investigation, Software, Formal Analysis, Writing - Original Draft. **Sili Deng:** Conceptualization, Project Administration, Writing - Review and Editing.

[1] Q. Wang, B. Mao, S. I. Stoliarov, J. Sun, A review of lithium ion battery failure mechanisms and fire prevention strategies, *Progress in Energy and Combustion Science* 73 (2019) 95–131. doi:10.1016/j.pecs.2019.03.002.

[2] Y. Wang, D. Ren, X. Feng, L. Wang, M. Ouyang, Thermal kinetics comparison of delithiated $\text{Li}[\text{Ni}_x\text{Co}_y\text{Mn}_{1-x-y}]\text{O}_2$ cathodes, *Journal of Power Sources* 514 (2021) 230582. doi:10.1016/j.jpowsour.2021.230582.

[3] B. C. Koenig, P. Zhao, S. Deng, Accommodating physical reaction schemes in DSC cathode thermal stability analysis using chemical reaction neural networks, *Journal of Power Sources* 581 (2023) 233443. doi:10.1016/j.jpowsour.2023.233443.

[4] B. C. Koenig, H. Chen, Q. Li, P. Zhao, S. Deng, Uncertain lithium-ion cathode kinetic decomposition modeling via Bayesian chemical reaction neural networks, *Proceedings of the Combustion Institute* 40 (1) (2024) 105243. doi:10.1016/j.proci.2024.105243.

[5] A. Kriston, I. Adanouj, V. Ruiz, A. Pfrang, Quantification and simulation of thermal decomposition reactions of Li-ion battery materials by simultaneous thermal analysis coupled with gas analysis, *Journal of Power Sources* 435 (2019) 226774. doi:10.1016/j.jpowsour.2019.226774.

[6] D. Ren, X. Liu, X. Feng, L. Lu, M. Ouyang, J. Li, X. He, Model-based thermal runaway prediction of lithium-ion batteries from kinetics analysis of cell components, *Applied Energy* 228 (2018) 633–644. doi:10.1016/j.apenergy.2018.06.126.

[7] B. C. Koenig, P. Zhao, S. Deng, Comprehensive thermal-kinetic uncertainty quantification of lithium-ion battery thermal runaway via bayesian chemical reaction neural networks, *Chemical Engineering Journal* 507 (2025) 160402. doi:<https://doi.org/10.1016/j.cej.2025.160402>.

[8] H. E. Kissinger, Variation of peak temperature with heating rate in differential thermal analysis, *Journal of Research of the National Bureau of Standards* 57 (4) (1956) 217. doi:10.6028/jres.057.026.

[9] D. D. MacNeil, J. R. Dahn, The Reactions of $\text{Li}_{0.5}\text{CoO}_2$ with Nonaqueous Solvents at Elevated Temperatures, *Journal of The Electrochemical Society* 149 (7) (2002) A912. doi:10.1149/1.1483865.

[10] S. Vyazovkin, A. K. Burnham, J. M. Criado, L. A. Pérez-Maqueda, C. Popescu, N. Sbirrazzuoli, ICTAC Kinetics Committee recommendations for performing kinetic computations on thermal analysis data, *Thermochimica Acta* 520 (1) (2011) 1–19. doi:10.1016/j.tca.2011.03.034.

[11] S. Vyazovkin, Kissinger Method in Kinetics of Materials: Things to Beware and Be Aware of, *Molecules* (Basel, Switzerland) 25 (12) (2020) E2813. doi:10.3390/molecules25122813.

[12] W. Ji, S. Deng, Autonomous Discovery of Unknown Reaction Pathways from Data by Chemical Reaction Neural Network, *The Journal of Physical Chemistry A* 125 (4) (2021) 1082–1092. doi:10.1021/acs.jpca.0c09316.

[13] S. Bhatnagar, A. Comerford, Z. Xu, D. B. Polato, A. Banaeizadeh, A. Ferraris, Chemical Reaction Neural Networks for fitting Accelerating Rate Calorimetry data, *Journal of Power Sources* 628 (2025) 235834. doi:10.1016/j.jpowsour.2024.235834.

[14] J. Zhang, C. Ma, S. Liu, Q. Guo, S. Liu, P. Han, Z. Huang, D. Han, Chemical reaction neural networks to map lithium-ion battery thermal runaway gas generation, *Cell Reports Physical Science* 6 (5) (May 2025). doi:10.1016/j.xcrp.2025.102563.

[15] X. Feng, X. He, M. Ouyang, L. Lu, P. Wu, C. Kulp, S. Prasser, Thermal runaway propagation model for designing a safer battery pack with 25Ah $\text{Li}[\text{Ni}_x\text{Co}_y\text{Mn}_z\text{O}_2]$ large format lithium ion battery, *Applied Energy* 154 (2015) 74–91. doi:10.1016/j.apenergy.2015.04.118.

[16] A. Kvasha, C. Gutiérrez, U. Osa, I. de Meataz, J. A. Blazquez, H. Maciior, I. Urdampilleta, A comparative study of thermal runaway of commercial lithium ion cells, *Energy* 159 (2018) 547–557. doi:10.1016/j.energy.2018.06.173.

[17] Y. P. Stenzel, M. Börner, Y. Preibisch, M. Winter, S. Nowak, Thermal profiling of lithium ion battery electrodes at different states of charge and aging conditions, *Journal of Power Sources* 433 (2019) 226709. doi:10.1016/j.jpowsour.2019.226709.

[18] Z. Cui, C. Liu, F. Wang, A. Manthiram, Navigating thermal stability intricacies of high-nickel cathodes for high-energy lithium batteries, *Nature Energy* 10 (4) (2025) 490–501. doi:10.1038/s41560-025-01731-x.

[19] A. Karmakar, H. Zhou, B. S. Vishnugopi, J. A. Jeevarajan, P. P. Mukherjee, State-of-Charge Implications of Thermal Runaway in Li-ion Cells and Modules, *Journal of The Electrochemical Society* 171 (1) (2024) 010529. doi:10.1149/1945-7111/adiecc.

[20] T. He, T. Zhang, S. Gadkari, Z. Wang, N. Mao, Q. Cai, An investigation on thermal runaway behaviour of a cylindrical lithium-ion battery under different states of charge based on thermal tests and a three-dimensional thermal runaway model, *Journal of cleaner production* 388 (2023) 135980. doi:10.1016/j.jclepro.2023.135980.

[21] D. J. Xiong, L. D. Ellis, J. Li, H. Li, T. Hynes, J. P. Allen, J. Xia, D. S. Hall, I. G. Hill, J. R. Dahn, Measuring Oxygen Release from Delithiated $\text{LiNi}_x\text{Mn}_y\text{Co}_{1-x-y}\text{O}_2$ and Its Effects on the Performance of High Voltage Li-Ion Cells, *Journal of The Electrochemical Society* 164 (13) (2017) A3025. doi:10.1149/2.0291713jes.

[22] S.-K. Jung, H. Gwon, J. Hong, K.-Y. Park, D.-H. Seo, H. Kim, J. Hyun, W. Yang, K. Kang, Understanding the Degradation Mechanisms of $\text{LiNi}_{0.5}\text{Co}_{0.2}\text{Mn}_{0.3}\text{O}_2$ Cathode Material in Lithium Ion Batteries, *Advanced Energy Materials* 4 (1) (2014) 1300787. doi:10.1002/aem.201300787.

[23] R. Jung, M. Metzger, F. Maglia, C. Stinner, H. A. Gasteiger, Chemical versus Electrochemical Electrolyte Oxidation on NMC111, NMC622, NMC811, LNMO, and Conductive Carbon, *The Journal of Physical Chemistry Letters* 8 (19) (2017) 4820–4825. doi:10.1021/acs.jpcllett.7b01927.

[24] S.-M. Bak, K.-W. Nam, W. Chang, X. Yu, E. Hu, S. Hwang, E. A. Stach, K.-B. Kim, K. Y. Chung, X.-Q. Yang, Correlating Structural Changes and Gas Evolution during the Thermal Decomposition of Charged $\text{Li}_x\text{Ni}_{0.8}\text{Co}_{0.15}\text{Al}_{0.05}\text{O}_2$ Cathode Materials, *Chemistry of Materials* 25 (3) (2013) 337–351. doi:10.1021/cm303096e.

[25] R. Jung, M. Metzger, F. Maglia, C. Stinner, H. A. Gasteiger, Oxygen Release and Its Effect on the Cycling Stability of $\text{Li}_{x}\text{Mn}_y\text{Co}_z\text{O}_2$ (NMC) Cathode Materials for Li-Ion Batteries, *Journal of The Electrochemical Society* 164 (7) (2017) A1361. doi:10.1149/2.0021707jes.

[26] B. C. Koenig, S. Deng, Kolmogorov-arnold chemical reaction neural networks for learning pressure-dependent kinetic rate laws, *arXiv preprint arXiv:2511.07686* (2025).

[27] Z. Liu, Y. Wang, S. Vaidya, F. Ruehle, J. Halverson, M. Soljačić, T. Y. Hou, M. Tegmark, KAN: Kolmogorov-Arnold NetworksArXiv preprint arXiv:2404.19756 (2024).

[28] B. C. Koenig, S. Kim, S. Deng, LeanKAN: a parameter-lean Kolmogorov-Arnold network layer with improved memory efficiency and convergence behavior, *Neural Networks* 192 (2025) 107883. doi:10.1016/j.neunet.2025.107883.

[29] B. C. Koenig, S. Kim, S. Deng, KAN-ODEs: Kolmogorov–Arnold network ordinary differential equations for learning dynamical systems and hidden physics, *Computer Methods in Applied Mechanics and Engineering* 432 (2024) 117397. [doi:10.1016/j.cma.2024.117397](https://doi.org/10.1016/j.cma.2024.117397).

[30] B. C. Koenig, S. Kim, S. Deng, ChemKANs for combustion chemistry modeling and acceleration, *Physical Chemistry Chemical Physics* (Jul. 2025). [doi:10.1039/D5CP02009C](https://doi.org/10.1039/D5CP02009C).

[31] R. T. Q. Chen, Y. Rubanova, J. Bettencourt, D. Duvenaud, Neural Ordinary Differential Equations, *arXiv preprint arXiv:1806.07366* (2019).

[32] S.-M. Bak, E. Hu, Y. Zhou, X. Yu, S. D. Senanayake, S.-J. Cho, K.-B. Kim, K. Y. Chung, X.-Q. Yang, K.-W. Nam, Structural Changes and Thermal Stability of Charged $\text{LiNi}_x\text{Mn}_y\text{Co}_z\text{O}_2$ Cathode Materials Studied by Combined *In Situ* Time-Resolved XRD and Mass Spectroscopy, *ACS Applied Materials & Interfaces* 6 (24) (2014) 22594–22601. [doi:10.1021/am506712c](https://doi.org/10.1021/am506712c).

[33] S. Sharifi-Asl, J. Lu, K. Amine, R. Shahbazian-Yassar, Oxygen release degradation in li-ion battery cathode materials: mechanisms and mitigating approaches, *Advanced Energy Materials* 9 (22) (2019) 1900551. [doi:10.1002/aem.201900551](https://doi.org/10.1002/aem.201900551).

[34] I. Belharouak, D. Vissers, K. Amine, Thermal stability of the li (ni0. 8co0. 15al0. 05) o2 cathode in the presence of cell components, *Journal of The Electrochemical Society* 153 (11) (2006) A2030. [doi:10.1149/1.2336994](https://doi.org/10.1149/1.2336994).

[35] P. Ping, Q. Wang, P. Huang, J. Sun, C. Chen, Thermal behaviour analysis of lithium-ion battery at elevated temperature using deconvolution method, *Applied energy* 129 (2014) 261–273. [doi:10.1016/j.apenergy.2014.04.092](https://doi.org/10.1016/j.apenergy.2014.04.092).

[36] Q. Wang, P. Ping, X. Zhao, G. Chu, J. Sun, C. Chen, Thermal runaway caused fire and explosion of lithium ion battery, *Journal of power sources* 208 (2012) 210–224. [doi:10.1016/j.jpowsour.2012.02.038](https://doi.org/10.1016/j.jpowsour.2012.02.038).

[37] M. Henriksen, K. Vågsæther, J. Lundberg, S. Forseth, D. Bjerketvedt, Explosion characteristics for li-ion battery electrolytes at elevated temperatures, *Journal of hazardous materials* 371 (2019) 1–7. [doi:10.1016/j.jhazmat.2019.02.108](https://doi.org/10.1016/j.jhazmat.2019.02.108).

[38] D. Zhuang, M. Z. Bazant, Theory of Layered-Oxide Cathode Degradation in Li-ion Batteries by Oxidation-Induced Cation Disorder, *Journal of The Electrochemical Society* 169 (10) (2022) 100536. [doi:10.1149/1945-7111/ac9a09](https://doi.org/10.1149/1945-7111/ac9a09).

[39] Y. Zhang, Y. Katayama, R. Tatara, L. Giordano, Y. Yu, D. Fragedakis, J. G. Sun, F. Maglia, R. Jung, M. Z. Bazant, Y. Shao-Horn, Revealing electrolyte oxidation via carbonate dehydrogenation on Ni-based oxides in Li-ion batteries by *in situ* Fourier transform infrared spectroscopy, *Energy & Environmental Science* 13 (1) (2020) 183–199. [doi:10.1039/C9EE02543J](https://doi.org/10.1039/C9EE02543J).

[40] H. F. Xiang, H. Wang, C. H. Chen, X. W. Ge, S. Guo, J. H. Sun, W. Q. Hu, Thermal stability of LiPF_6 -based electrolyte and effect of contact with various delithiated cathodes of Li-ion batteries, *Journal of Power Sources* 191 (2) (2009) 575–581. [doi:10.1016/j.jpowsour.2009.02.045](https://doi.org/10.1016/j.jpowsour.2009.02.045).

[41] L. Wang, T. Maxisch, G. Ceder, A First-Principles Approach to Studying the Thermal Stability of Oxide Cathode Materials, *Chemistry of Materials* 19 (3) (2007) 543–552. [doi:10.1021/cm0620943](https://doi.org/10.1021/cm0620943).

[42] S. SS, K. AR, A. KP, et al., Chebyshev polynomial-based kolmogorov-arnold networks: An efficient architecture for nonlinear function approximation, *arXiv preprint arXiv:2405.07200* (2024).

[43] C. Rackauckas, Q. Nie, DifferentialEquations.jl – A Performant and Feature-Rich Ecosystem for Solving Differential Equations in Julia, *Journal of Open Research Software* 5 (1) (2017) 15. [doi:10.5334/jors.151](https://doi.org/10.5334/jors.151).

[44] J. Revels, M. Lubin, T. Papamarkou, Forward-Mode Automatic Differentiation in Julia, *arXiv preprint arXiv:1607.07892* (2016).

[45] D. P. Kingma, J. Ba, Adam: A Method for Stochastic Optimization, *arXiv preprint arXiv:1412.6980* (Jan. 2017).

[46] W. Li, S. Lee, A. Manthiram, High-nickel NMA: a cobalt-free alternative to NMC and NCA cathodes for lithium-ion batteries, *Advanced materials* 32 (33) (2020) 2002718. [doi:10.1002/adma.202002718](https://doi.org/10.1002/adma.202002718).

[47] Q. Li, H. Chen, B. C. Koenig, S. Deng, Bayesian chemical reaction neural network for autonomous kinetic uncertainty quantification, *Physical Chemistry Chemical Physics* 25 (5) (2023) 3707–3717. [doi:10.1039/D2CP05083H](https://doi.org/10.1039/D2CP05083H).

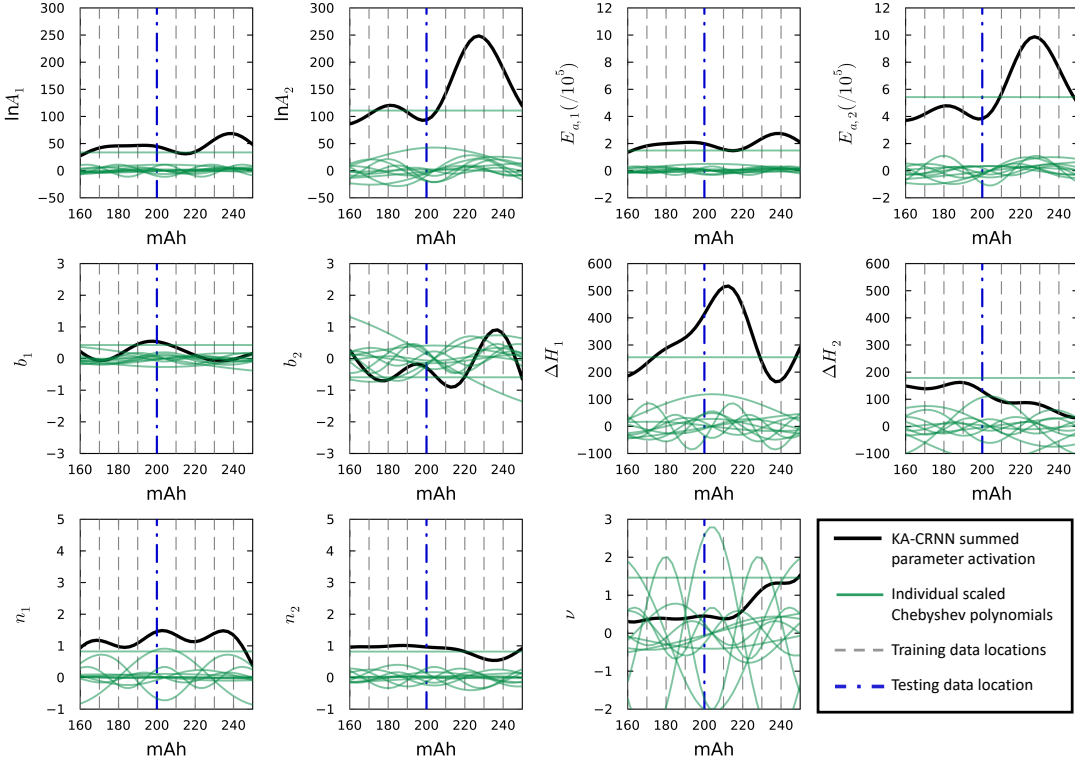


FIG. A1: Learned KA-CRNN activations for the NM cathode. Individual green Chebyshev polynomials sum to the black KA-CRNN parameter functions.

APPENDIX A. KA-CRNN ACTIVATIONS FOR NCM AND NM CATHODES

KA-CRNN activations are provided here for all kinetic parameters of all three studied cathodes (Figs. A1, A2, and A3). Comparison across these activations reveals similar qualitative trends despite the differences across cathodes in the reconstructed DSC results in Fig. 3. A key behavior not previously discussed in Fig. 4 is that of ΔH_1 . In all three cathodes, it follows a trend of increasing enthalpy up to 200 mAh, then a noticeable decrease toward the critical SOC. The decrease toward higher SOCs appears counterintuitive, as it is well known (and also demonstrated in the current work) that the thermal stability of these cathode materials decreases with increased SOCs. Interestingly, a close inspection of the training data reveals that R1 does not appear to follow this trend, and in fact in many cases releases more total heat at intermediate SOCs, rather than at the critical SOC and above. For the NM cathode, for example, the R1 peak heat release rate at 210 mAh is 33% higher than that at 220 mAh, while for the NCA cathode the 213 mAh peak is 21% higher than the 224 mAh peak. It is not clear from the current results whether this is a true chemical behavior or an artifact of the experimental methods, but in either case it is clear that the behavior learned by the KA-CRNN, whether expected or unexpected, can be traced directly to behaviors present in the underlying training data.

APPENDIX B. KA-CRNN DATA RECONSTRUCTIONS AT REMAINING STATES OF CHARGE

The results in Fig. 3 show only three reconstructed data profiles for each cathode, to facilitate concise discussion. In this appendix we report all reconstructed data profiles: the NM cathode in Fig. B1, NMA in Fig. B2, and finally NCA in Fig. B3.

APPENDIX C. SUPPLEMENTARY DATA

Supplementary material is available for this article.

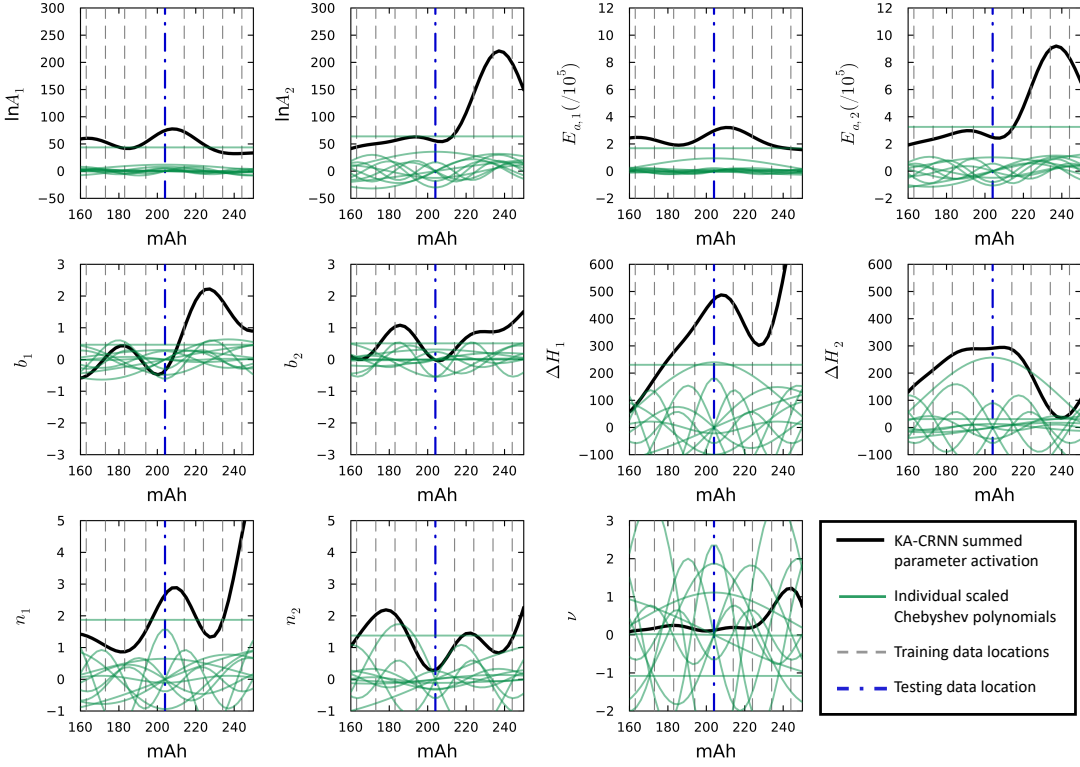


FIG. A2: Learned KA-CRNN activations for the NMA cathode. Individual green Chebyshev polynomials sum to the black KA-CRNN parameter functions.

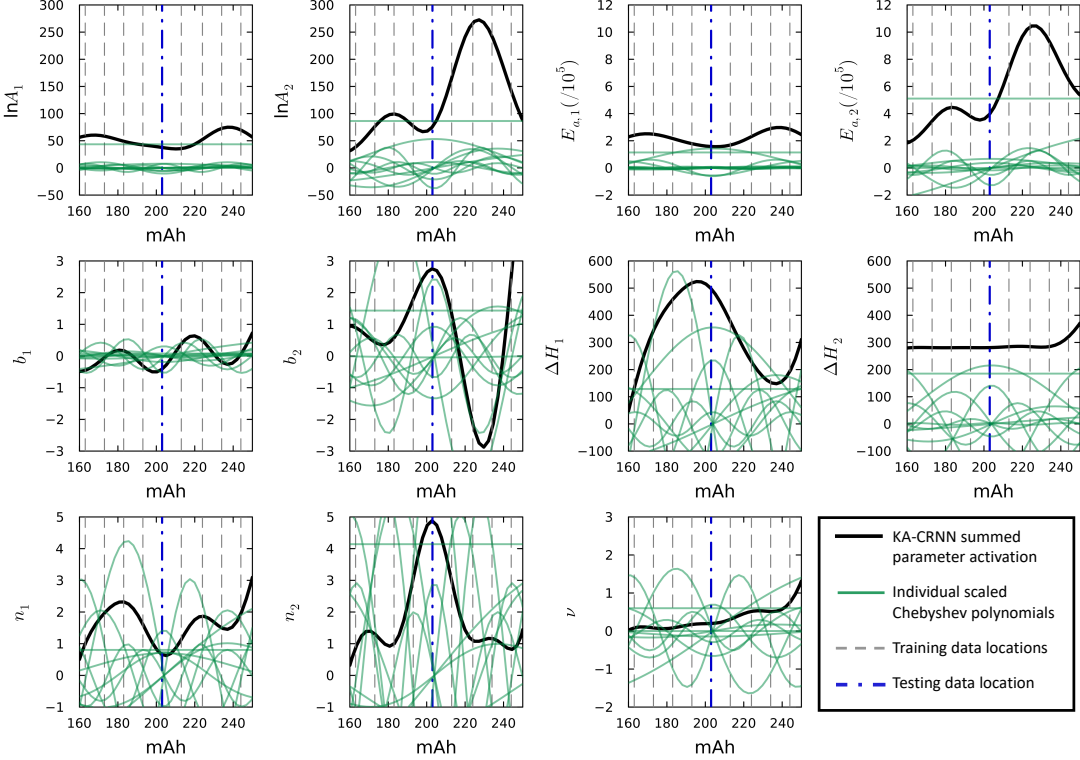


FIG. A3: Learned KA-CRNN activations for the NCA cathode. Individual green Chebyshev polynomials sum to the black KA-CRNN parameter functions.

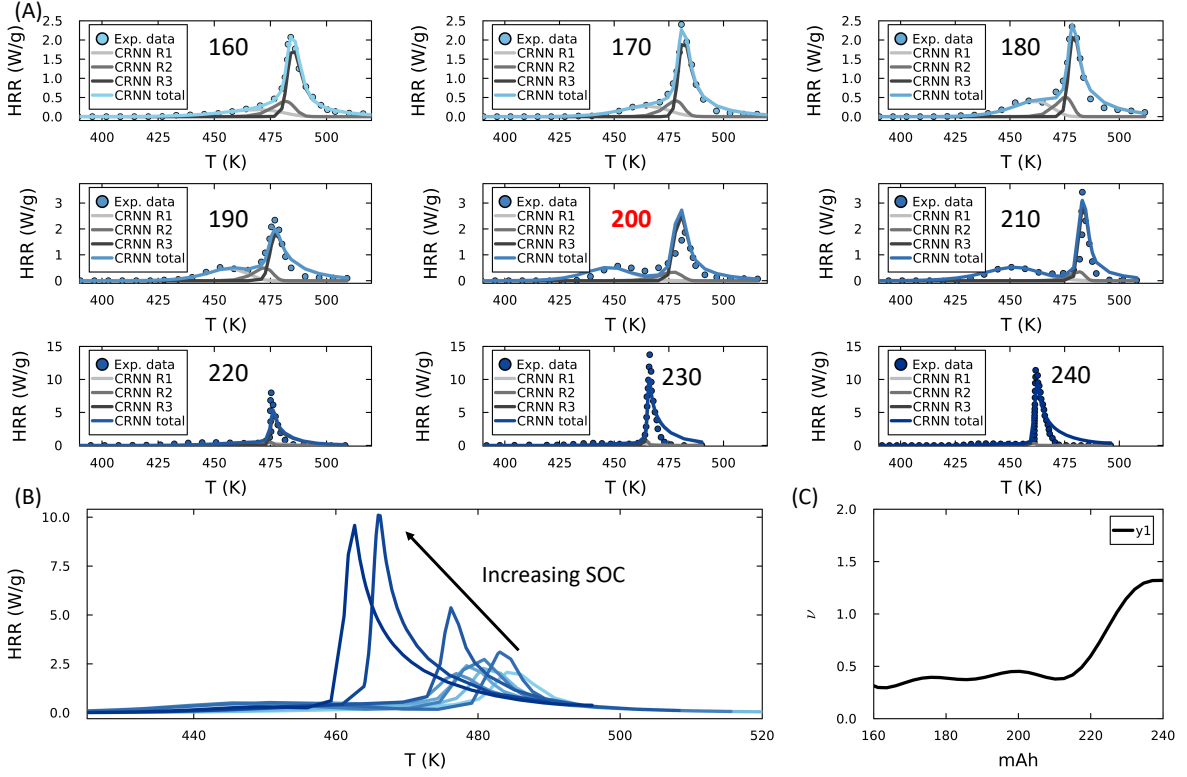


FIG. B1: (A) NM DSC reconstructions at all SOCs (train/test). (B) All reconstructions plotted together to visualize SOC effect. (C) Oxygen stoichiometric coefficient KA-CRNN activation, highlighting critical SOC.

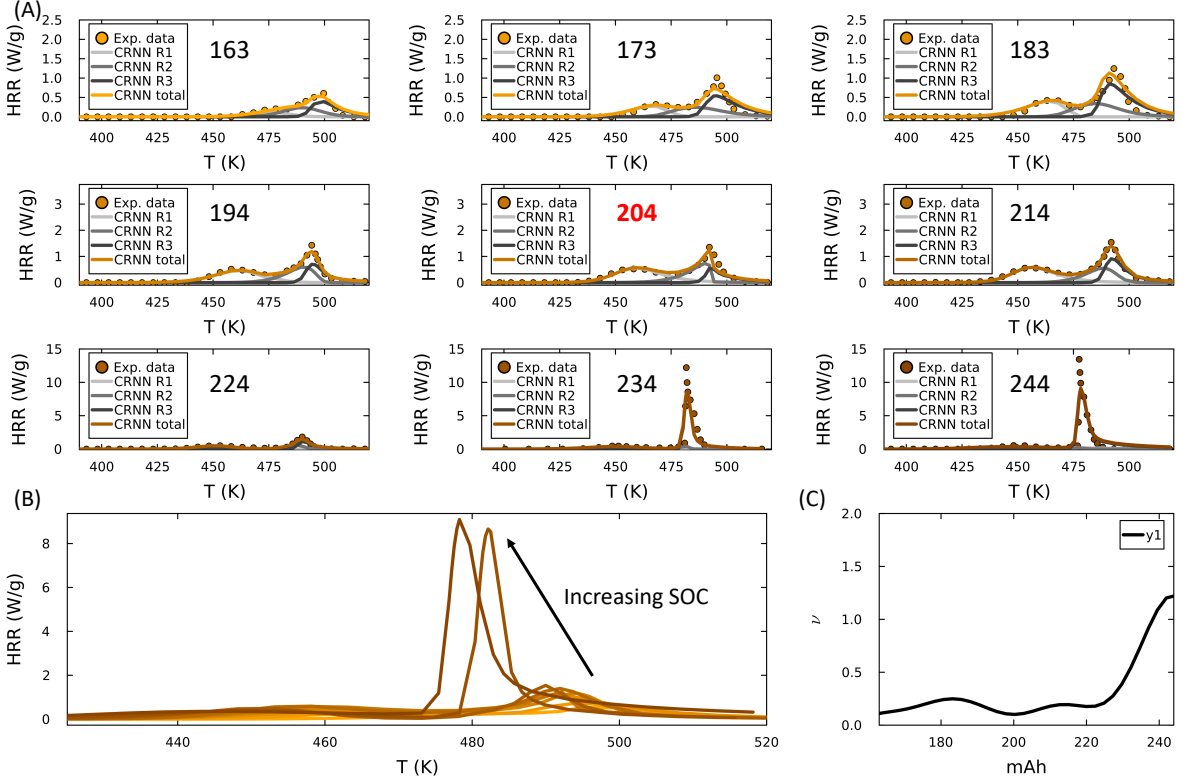


FIG. B2: (A) NMA DSC reconstructions at all SOCs (train/test). (B) All reconstructions plotted together to visualize SOC effect. (C) Oxygen stoichiometric coefficient KA-CRNN activation, highlighting critical SOC.

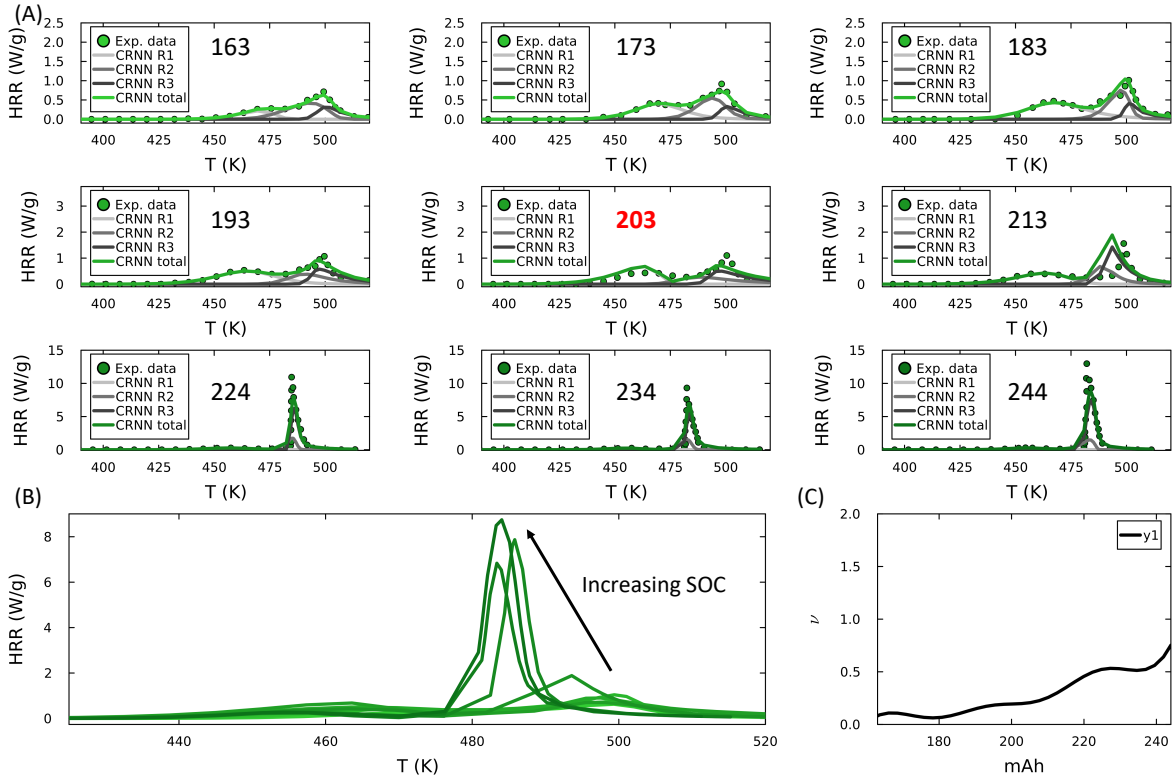


FIG. B3: (A) NCA DSC reconstructions at all SOCs (train/test). (B) All reconstructions plotted together to visualize SOC effect. (C) Oxygen stoichiometric coefficient KA-CRNN activation, highlighting critical SOC.